Boundary-Layer Meteorology (2023) 186:27–41
https://doi.org/10.1007/s10546-022-00740-7

RESEARCH ARTICLE

Inclination Angles of Turbulent Structures in Stably Stratified Boundary Layers

Jeremy A. Gibbs[1] · **Rob Stoll**[2] · **Scott T. Salesky**[3]

Received: 11 April 2022 / Accepted: 6 August 2022 / Published online: 3 October 2022

Abstract

There is a rich history of studying coherent structures in the atmospheric boundary layer through the use of spatial correlations between wall shear stress and elevated velocity measurements. This work has primarily focused on neutral and convective boundary layers, while structures in the stable boundary layer (SBL) have received less attention. We use direct numerical simulations (DNSs) of turbulent channel flow across a range of static stabilities to examine the inclination angles of turbulent structures in the SBL. Angles are inferred not only from wall shear stress and velocity correlations, but also from correlations between the wall buoyancy flux and buoyancy. Results indicate that structures in the SBL have a smaller angle than those under neutral conditions, and that the difference is enhanced with increasing stratification. Specifically, stratification across the range of considered simulations decreases the angles from the neutral case by $< 1°$ near the surface and by $\sim$ 1–3° at the top of the logarithmic region. Additionally, the angles of buoyancy structures are larger than those inferred from momentum by $\sim 3°$ throughout the entire depth of this layer. Further, angles increase with height until leveling off near the top of the logarithmic region, which may be the result of local z-less stratification based on analysis of the Richardson number and normalized standard deviations. The DNS data are in good agreement with both existing published data and newly reported observations from the AHATS field campaign. Both numerical and observational data exhibit an increase in angle variability with increasing stratification, which seemingly indicates that the variability is related to physical processes of the flow, such as intermittency or laminarization/bursting phenomena. In the future, large-eddy

✉ Jeremy A. Gibbs
jeremy.gibbs@noaa.gov

Rob Stoll
rstoll@eng.utah.edu

Scott T. Salesky
salesky@ou.edu

[1] NOAA/OAR National Severe Storms Laboratory, 120 David L. Boren Blvd., Norman, OK 73072, USA

[2] Department of Mechanical Engineering, University of Utah, Salt Lake City, UT 84112, USA

[3] School of Meteorology, University of Oklahoma, Norman, OK 73072, USA

simulation surface boundary conditions will need to better capture this variability to properly represent instantaneous land-surface interactions in the SBL.

Keywords Stable boundary layer · Turbulence · DNS · Channel flow

1 Introduction

The form and properties of coherent structures in the atmospheric boundary layer (ABL) and other high-Reynolds (Re) number turbulent wall-bounded flows have been of continuous interest since the work of Richardson (1922). A particular focus has been the interaction of these structures with the wall and how this interaction translates forces between the wall and the fluid. Early experimental work sought to use spatial correlations between a wall shear probe and elevated velocity probes in a wind tunnel to understand how the large scale outer flow controls flow interactions with the wall in a turbulent boundary layer (Brown and Thomas 1977; Rajagopalan and Antonia 1979). These studies established that the correlation between the wall shear stress and the streamwise velocity decreases with height and that at a given height it is maximum along a lag or horizontal distance between the surface and overlying sensors (interpreted through Taylor's hypothesis) along a line inclined at between 12°–18° from the wall.

The inclination in the maximum correlation observed in these early studies has been confirmed and expanded beyond laboratory work to include numerical simulations and atmospheric observations (Piomelli et al. 1989; Boppe et al. 1999; Marusic et al. 2001; Carper and Porté-Agel 2004; Marusic and Heuer 2007; Chauhan et al. 2013). For neutrally stratified flow, these studies are consistent with prior observations. A few studies have also included unstably or stably stratified conditions. Based on sonic anemometer data from the atmospheric surface layer, Carper and Porté-Agel (2004) used conditional sampling techniques to identify hairpin like structures consistent with the hairpin packets of Adrian (2007), and based on cross-correlation between sensors at different heights presented results suggesting that the inclination angle of these structures increased under unstable conditions and was likely suppressed under stable conditions. Marusic and Heuer (2007) used direct measurements of surface shear stress from a custom designed sensor (Heuer and Marusic 2005) combined with sonic anemometers and calculated the cross-correlation between the two providing further evidence of the increase in inclination for unstable conditions. While only limited data on stable conditions was presented, they suggested that inclination angles in such environments are either similar or smaller than those found for near-neutral conditions. A more extensive study using an array of sonic anemometers by Chauhan et al. (2013) found similar inclination angles to past work for near-neutral conditions, but noted that discrepancies between closely spaced sensors and those that were placed farther apart suggested inclination could be a function of scale and that caution should be taken when interpreting angles based on the cross-correlation between sensors at different heights. The assertion of scale dependence supported earlier analysis of wind-tunnel data by Venugopal et al. (2003) who showed that the correlation between surface shear stress and velocity in the surface layer depends on the filter scale of the velocity field. Chauhan et al. (2013) also examined the impact of stability on the correlation between near surface turbulent momentum flux and velocity in the surface layer. They found a clear dependence that tracked the Obukhov length scale (L) for unstable conditions and a marked decrease in angle for stable conditions, although the stable conditions did not appear to follow a particular trend with Monin–Obukhov similarity theory

(MOST; Monin and Obukhov 1954). The trend was especially pronounced for unstable conditions where the angle implied through velocity correlations increased from its neutral value of $\gamma \approx 15°$ to as large as 45° under convective conditions. Liu et al. (2017) used a similar experimental setup to Chauhan et al. (2013) at a different location and confirmed both the structure inclination angle under neutral conditions and the dependence of the angle on L for convective conditions. Using hotwire anemometry Lotfy and Harun (2018) also confirmed prior observations for neutral and convective conditions. Yet under stable conditions they counter-intuitively found that the inclination angle increased consistently with increasing stability. This was attributed to a decrease in horizontal length scales under strongly stratified conditions.

More recently, researchers have used the large-eddy simulation (LES) technique (Stoll et al. 2020) to examine the structure of turbulence and the average inclination angle of structures deduced from two-point correlations for a variety of atmospheric stability conditions. Based on a suite of simulations with forcings ranging from weak to strong unstable stratification, Salesky and Anderson (2018) demonstrated that the average inclination angle of structures increases from its neutral value of $\sim$15° to nearly vertical as the flow approached free convection. The transition from mostly horizontal to nearly vertical correlations was associated with the transition in flow structures from shear-dominated inclined structures to nearly vertical buoyant plumes. Salesky and Anderson (2020) followed up on this work to develop a model to predict the inclination angle as a function of atmospheric stability from neutral to convective conditions. The change in inclination angle was demonstrated to result from the downstream uplift of inclined wall structures by buoyancy forces resulting in structures consisting of a vertical region with an inclination dependent on stability overlaying a distinctly different momentum region that is dominated by shear. Similar to experimental inquiries, evidence and theory on the inclination angle of structures under stably stratified conditions based on simulations is sparse. Although not based on correlations, Sullivan et al. (2016) examined the inclination angle of temperature fronts in the stable boundary layer using LES. They found that the inclination angle decreased with increasing stratification and that the angle itself is dependent on the spacing between and strength of inclined vortical structures associated with the temperature front.

This study seeks to fill the gap in the literature on the inclination of turbulent flow structures under stable stratification. Specifically, we seek to better understand the response of inclination angles to stratification, and to quantify the range and variability of inclination angles in stable flows through both numerical and observational data. To that end, a series of direct numerical simulations (DNSs) of turbulent channel flow with different levels of imposed stratification are used to explore the mean inclination angle of turbulent flow structures associated with the creation of surface shear stress and buoyancy flux. Complementary results from atmospheric surface layer observations are also presented. A summary of a suite of DNSs is given in Sect. 2, results are presented in Sect. 3, and our main conclusions are given in Sect. 4.

2 Methods

2.1 Numerical Experiments

We performed DNSs of five turbulent channel-flow cases across a range of static stability values to investigate the impact of stratification on momentum and buoyancy structures.

Each simulation domain encompassed a full channel, so only data from the lower-half of the channel were considered for analyses. Simulations were carried out on the National Center for Atmospheric Research (NCAR) Cheyenne supercomputer (Computational and Information Systems Laboratory 2019) using the open-source computational fluid dynamics code MicroHH (van Heerwaarden et al. 2017). The governing flow equations were spatially discretized and solved numerically with fourth-order finite differencing of the advection and diffusion terms, a fourth-order Poisson solver was used for pressure, and a third-order Runge–Kutta scheme was applied for the time integration. Grid stretching was applied in the vertical direction using a hyperbolic tangent function. Further details about the numerical grid configuration are given in Table 1. The flow was driven by a constant large-scale streamwise pressure gradient $-\rho^{-1}\nabla_x p = 10^{-4}$ m s^{-2}. The lower and upper boundary conditions were no-slip for velocity (where $\{u, v, w\}$ are the respective velocity components along the streamwise (x), spanwise (y) and vertical (z) coordinate directions). For scalars, we operate in the buoyancy framework instead of temperature, with buoyancy $b(x, y, z) = g\left[\Theta(x, y, z) - \overline{\Theta}(z)\right]/\Theta_r$, where g is acceleration due to gravity, $\Theta(x, y, z)$ is the potential temperature at point x, y, z, $\overline{\Theta}(z)$ is the mean potential temperature at height z, and Θ_r is a constant reference potential temperature. Dirichlet boundary conditions for buoyancy were applied at each surface to ensure a constant stratification across the full channel (see Table 2). Lateral boundary conditions for all prognostic fields were periodic.

The numerical experiments were in the spirit of those reported by Moser et al. (1999) and García-Villalba and del Álamo (2011) and extended to a target friction Reynolds number $Re_\tau = hu_\tau/\nu \approx 1000$ for the neutral case, where h is the boundary layer depth (defined as the height where the turbulent component of the total vertical momentum flux is first eclipsed by the diffusive component; see Table 2), $u_\tau \approx 0.01$ m s^{-1} is friction velocity, and $\nu = 10^{-5}$ m^2 s^{-1} is kinematic viscosity. The cited works use the channel half-height δ as the vertical scale, while we instead use h since it is more physically relevant under the stable stratification present in this study. The five simulations were conducted as a set of consecutive runs. The neutral case A1 was initialized with two pairs of counter-rotating vortices aligned in the streamwise direction. Convergence was assumed when the profile of total shear stress was linear and the velocity field was quasi-steady (Kim et al. 1987; Vinuesa et al. 2016). The simulation was run until reaching a sufficient number of eddy turnover times $T_e = h/u_\tau$ beyond convergence over which to compute statistics. The total non-dimensional run time is expressed as $T_t^+ = T_c^+ + T_a^+ = (t_c + t_a)/T_e$, where t_c and t_a are the convergence time and averaging time in seconds, respectfully. Information about T_t^+ and T_a^+ for each simulation is provided in Table 3. At the end of the simulation, the A1 fields served as input fields for the A2 simulation. Next the surface buoyancy was reduced according to Table 2 and the A2 simulation was run until reaching the appropriate T_t^+. The process was then repeated for each remaining simulation. Relevant mean profiles of each simulation are shown in Fig. 1.

Bulk parameters that characterize the flow in each simulation are given in Table 3. They include Re_τ and the friction Richardson number $Ri_\tau = h\Delta b/u_\tau^2$, where Δb is the buoyancy

Table 1 Grid configuration for all reported simulations

L_x/δ	L_y/δ	N_x	N_y	N_z	Δx^+	Δy^+	Δz^+
8π	3π	2560	1792	384	9.8	5.2	0.36–10

L_x and L_y are the streamwise and spanwise lengths of the channel, δ is the channel half-height, N_x, N_y, and N_z are the number of numerical grid points in the streamwise, spanwise, and wall-normal directions, while Δx^+, Δy^+, Δz^+ are the corresponding normalized grid spacings

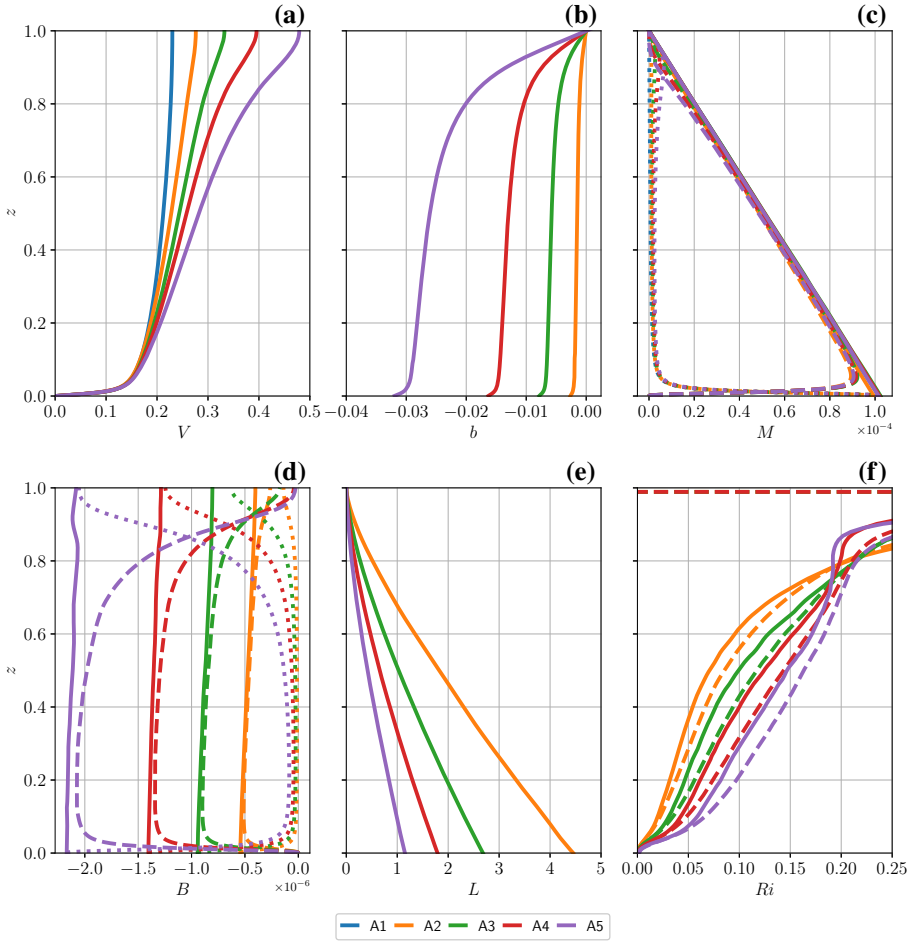

Fig. 1 Mean profiles of **a** velocity $V = \sqrt{u^2 + v^2}$ [m s^{-1}], **b** buoyancy [m s^{-2}], **c** momentum flux $M = (\overline{w'u'}^2 + \overline{w'v'}^2)^{0.5}$ [m^2 s^{-2}], **d** buoyancy flux $B = \overline{w'b'}$ [m^2 s^{-3}], **e** Obukhov length $L = -u_\tau^3/(\kappa \overline{w'b'})$ [m], and **f** the gradient Richardson number $Ri = (\partial b/\partial z)/((\partial u/\partial z)^2 + (\partial v/\partial z)^2)$ (solid) and flux Richardson number $Ri_f = (\overline{w'b'})/(\overline{w'u'}(\partial u/\partial z) + \overline{w'v'}(\partial v/\partial z))$ (dashed). In panels (**c**) and (**d**), dotted, dashed, and solid lines correspond to the diffusive, turbulent, and total flux values, respectively

Table 2 Forcing values of surface buoyancy b_o and boundary-layer depth h for all reported simulations. For reference, the channel half-height $\delta = 1$m

Case	b_o (m s^{-2})	h (m)
A1	0	0.989
A2	−0.002645	0.989
A3	−0.007840	0.956
A4	−0.016335	0.912
A5	−0.032000	0.879

Table 3 Bulk parameters

Case	Re_b	Re_τ	Ri_b	Ri_τ	Pr	Nu	C_f	T_t^+	T_a^+
A1	19,864	997	0.00	0	0.71	0.00	5.04	73.4	18.3
A2	21,548	986	0.06	26	0.71	14.45	4.19	36.3	18.1
A3	21,602	967	0.12	60	0.71	9.96	4.01	57.2	19.1
A4	20,660	921	0.18	91	0.71	8.88	3.98	79.7	19.9
A5	20,791	886	0.28	153	0.71	7.64	3.63	103.1	20.6

Subscripts b and τ refer to Reynolds numbers (Re) and Richardson numbers (Ri) based on the bulk velocity and surface shear stress, respectively. Pr is the Prandtl number, Nu is the Nusselt number, C_f is the friction coefficient, T_t^+ is the total normalized run time, and T_a^+ is the normalized time over which statistics were computed

change across the boundary layer, as well as their counterparts Re_b and Ri_b that are based on the bulk velocity u_b. Using Ri_b criteria from Grachev et al. (2013), A2–A4 represent *subcritical* turbulence regimes, while A5 falls under the *supercritical* regime—albeit within the range where some measure of small-scale turbulence may persist beyond the critical point. Additionally, Grachev et al. (2013) further divides the subcritical regime into the *surface-layer* regime (A2) and *local z-less* regime (A3 and A4), while the supercritical regime (A5) is called the *very stable* case. Similarly, A2 is considered *weakly stable* and A3–A5 are *transitional* according to Mahrt (1998) and Mauritsen and Svensson (2007). For all stratified simulations, the Prandtl number is imposed as $Pr = \nu/\nu_h = 0.71$, where $\nu_h = 1.41 \times 10^{-5}$ m^2 s^{-1} is thermal diffusivity. The Nusselt number $Nu = -h(\overline{w'b'})_o/(\nu_h \Delta b)$, where $(\overline{w'b'})_o$ is the surface vertical buoyancy flux, is a measure of the surface turbulent buoyant transport relative to its laminar state, which occurs at $Nu = 1$. The importance of the surface turbulent shear stress relative to the bulk shear across the half-channel is quantified by the friction coefficient $C_f = 2(u_\tau/u_b)^2$. As expected, there is a notable decrease in Nu and C_f with increasing stability. In our configuration, u_τ is approximately fixed because we hold $\nabla_x p$ constant (García-Villalba and del Álamo 2011), which means that the decrease in C_f is attributed to an acceleration of u_b. Finally, the presented total run times and averaging times for each simulation are normalized by T_e. The time to reach convergence for each simulation increased with increasing stability because the resultant transition phase between adjoining simulation states grew longer with each progressive change in surface buoyancy.

2.2 Cross-Correlations

A fundamental quantity used to study organized boundary-layer structures is the cross-correlation between fluctuating fields of interest (e.g., Brown and Thomas 1977). The idea is that there is some measure of correlation in the flow where the structures exist, and that the inferred angle computed from simple geometry using the measurement height and the distance (lag) that corresponds to the peak correlation will elucidate the obliqueness of such structures. These angles have proven useful for allowing one to construct models of the surface layer (Marusic and Heuer 2007). The most common cross-correlations are between the surface shear stress and the streamwise velocity, or between the streamwise velocity with itself (e.g., Brown and Thomas 1977; Marusic et al. 2001; Chauhan et al. 2013; Liu et al. 2017). In this study, we hypothesize that surface ejections (Quadrant II: $u' < 0$, $w' > 0$) and sweeps (Quadrant IV: $u' > 0$, $w' < 0$) are important in the stable surface layer (see, e.g.,

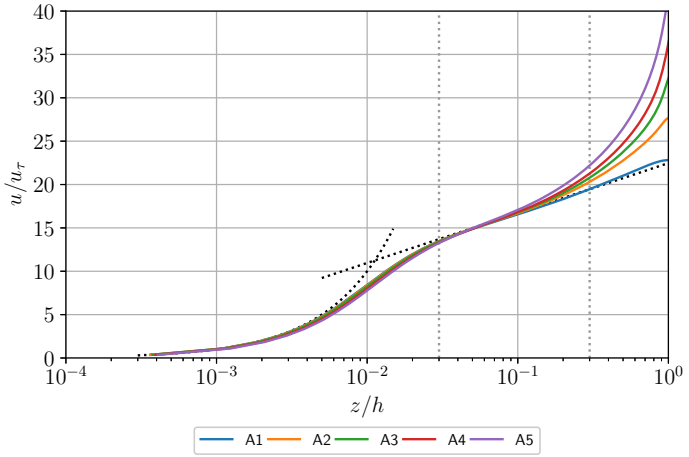

Fig. 2 Normalized velocity profiles. The vertical dashed gray lines indicate the region over which cross-correlations are computed. The dashed black lines indicate the theoretical linear and logarithmic profiles

Antonia 1981). Accordingly, we compute cross-correlations between the surface shear stress and the streamwise velocity, as well as between the surface buoyancy flux and buoyancy.

The definition of the cross-correlation between surface shear stress τ and streamwise velocity u with temporal lags is presented by (2007, Eq.1). The spatial equivalent of this cross-correlation as a function of height is defined as:

$$R_{\tau,u}(\Delta_r, z) = \frac{1}{(N_x N_y - 1)} \sum_{j=1}^{N_y} \sum_{i=1}^{N_x} \frac{[\tau(x_i, y_j) - \overline{\tau}][u(x_i + \Delta_r, y_j, z) - \overline{u}]}{\sigma_\tau \sigma_u}, \tag{1}$$

where N_x is the number of grid points in the streamwise direction, N_y is the number of grid points in the spanwise direction, Δ_r is the considered lag for $r \in \{-N_x/2, N_x/2\}$, overlines represents the horizontal planar mean for each field, and σ is the streamwise standard deviation of the quantity of interest. The surface shear stress is defined as:

$$\tau = \nu \sqrt{\left(\frac{\partial u}{\partial z}\right)^2 + \left(\frac{\partial v}{\partial z}\right)^2}\,|_{z=0}.$$

Similarly, the cross-correlation between surface buoyancy flux B and buoyancy b with height is defined as:

$$R_{B,b}(\Delta_r, z) = \frac{1}{(N_x N_y - 1)} \sum_{j=1}^{N_y} \sum_{i=1}^{N_x} \frac{[B(x_i, y_j) - \overline{B}][b(x_i + \Delta_r, y_j, z) - \overline{b}]}{\sigma_B \sigma_b}, \tag{2}$$

where the surface buoyancy flux is defined as:

$$B = -\nu_h \frac{\partial b}{\partial z}|_{z=0}. \tag{3}$$

The negative sign leading B results in negative cross-correlations. For consistency with $R_{\tau,u}$, we take the absolute value of $R_{B,b}$ and drop the bars for notational simplicity (i.e., $R_{B,b} = |R_{B,b}|$).

Procedurally, $R_{\tau,u}$ and $R_{B,b}$ are computed from a single snapshot using the surface stress/flux and their associated fields taken at a given height and lag in the log region. We identified the log region for case A1 using the theoretical considerations in Pope (2000), then applied those vertical bounds to all other cases. The percent difference between the DNS data and the theoretical logarithmic profile at the top of the log region is less than 1% in the neutral case, and approximately 12% in the A5 case (see Fig. 2). This process is repeated for all heights in the log region and for all considered lags across each of the 61 snapshots saved during the T_a^+ reported in Table 3, which were separated by $\approx 0.3T_e^+$. Finally, the inclination angle was computed as:

$$\gamma = \tan^{-1}\left(\frac{z}{\Delta_r^*}\right), \tag{4}$$

where z is height and Δ_r^* is the lag that corresponds with the maximum cross-correlation at height z.

3 Results

As a representative example, Fig. 3 shows cross-correlations $R_{\tau,u}$ (panel a) and $R_{B,b}$ (panel b) for the A2 case. Values are shown for a sample of seven heights in the logarithmic region of the boundary layer, chosen here as the range $0.03 \leq z/h \leq 0.30$. The maximum values of $R_{\tau,u}$ span the range of approximately 0.45 at $z/h = 0.03$ to 0.11 at $z/h = 0.30$, while the maximum values for $R_{B,b}$ span approximately 0.47 to 0.09 over the same depth. These values are reasonable based on the reported literature (e.g., Brown and Thomas 1977; Marusic et al. 2001). It is also apparent that the lag associated with the maximum value of the respective cross-correlations increases with increasing height. Compared with $R_{\tau,u}$, the $R_{B,b}$ distributions appear more asymmetric around the peak and constrained horizontally in lag space. This suggests that structures arising from buoyancy are at a larger angle with respect to the underlying surface than those arising from momentum.

The effects of differing stratification on the cross-correlations are seen in Fig. 4, where the maximum values of $R_{\tau,u}$ (panel a) and $R_{B,b}$ (panel b) are shown at the same selected heights as in Fig. 3. For both cross-correlations, every simulation exhibits a similar decrease away from the surface. The maximum value at a selected height decreases with increasing stratification, with the most pronounced difference being between the A1 and A2 cases for $R_{\tau,u}$ (there is no equivalent $R_{B,b}$ for case A1 due to neutral stratification). This suggests that structures are flattened relative to the vertical direction with increasing stratification. The spread in these differences increases with increasing height until $z/h = 0.15$, after which the differences relative to the imposed stratification remain fairly constant. Compared with $R_{\tau,u}$, the spread across cases is slightly smaller for $R_{B,b}$, suggesting that the buoyancy structures are slightly less affected by stratification than their momentum counterparts. This again implies that buoyancy structures have a larger inclination angle than momentum structures. Meanwhile, the maximum values of $R_{\tau,u}$ are slightly larger than those of $R_{B,b}$ at a given height above approximately $z/h = 0.05$.

The maximum values of $R_{\tau,u}$ and $R_{B,b}$ at a given height, along with the lag at which they occur, are used to compute the implied angle of the associated turbulent structures according to Eq. (4). These inclination angles based on $R_{\tau,u}$ (panel a) and $R_{B,b}$ (panel b) are shown in Fig. 5. Each angle computed using $R_{\tau,u}$ displays similar behavior across cases: the inclination angle increases rapidly in the lowest $z/h = 0.15$ and then levels off toward the top of the logarithmic region. Angles computed using $R_{B,b}$ exhibit similar behavior, except that there is

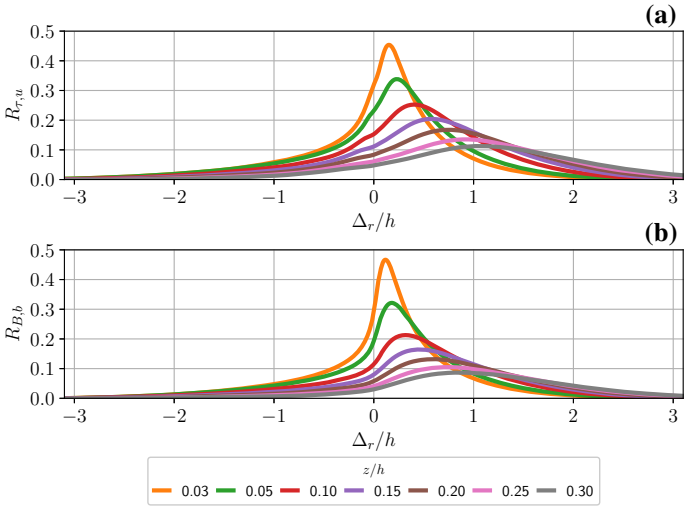

Fig. 3 Correlation coefficients **a** $R_{\tau,u}$ and **b** $R_{B,b}$ versus normalized spatial lag at various normalized heights for the A2 case

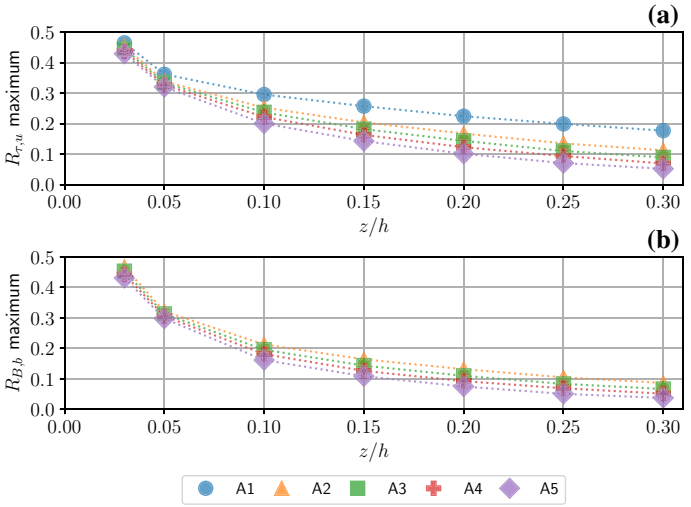

Fig. 4 Maximum correlation coefficients **a** $R_{\tau,u}$ and **b** $R_{B,b}$ as a function of normalized height

a slight decrease in the A5 case above $z/h = 0.20$. Given that the A5 case is in the *supercritical* regime, this behavior may indicate flow effects associated with non-Kolmogorov turbulence. Generally, the angles associated with both $R_{\tau,u}$ and $R_{B,b}$ decrease at a given height as stratification becomes stronger. For the shear-stress cross-correlations, $\gamma_{\mathrm{A2}} = 11.6°$ and $\gamma_{\mathrm{A5}} = 10.8°$ at $z/h = 0.03$, while $\gamma_{\mathrm{A2}} = 15.6°$ and $\gamma_{\mathrm{A5}} = 14.4°$ at $z/h = 0.30$. Similarly, for the buoyancy-flux cross-correlations, $\gamma_{\mathrm{A2}} = 14.4°$ and $\gamma_{\mathrm{A5}} = 14.3°$ at $z/h = 0.03$, while $\gamma_{\mathrm{A2}} = 19.4°$ and $\gamma_{\mathrm{A5}} = 16.9°$ at $z/h = 0.30$. Thus, stratification across the considered simulations affects γ by $< 1°$ near the surface and by $\sim$ 1–3° at the top of the logarithmic region. We can also define $\Delta_{B,\tau} = \gamma(R_{B,b}) - \gamma(R_{\tau,u})$ to understand how structures inferred

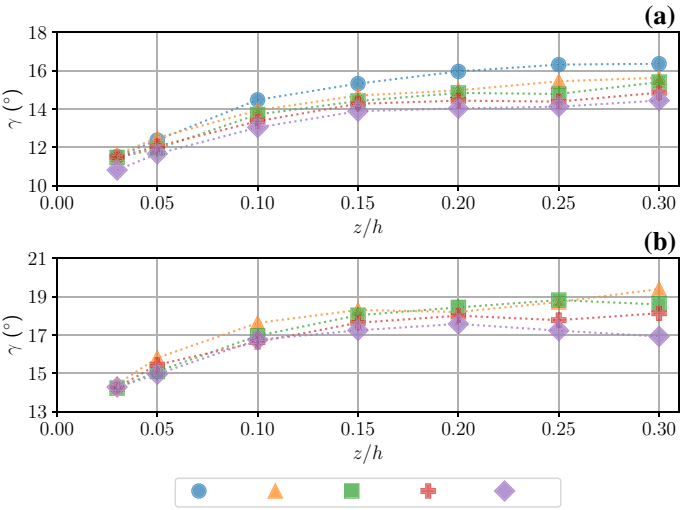

Fig. 5 Inclination angle as a function of normalized height based on **a** $R_{\tau,u}$ and **b** $R_{B,b}$

by their respective inclination angles differ. For the A2 case, $\Delta_{B,\tau} = 2.8°$ at $z/h = 0.03$ and $3.8°$ at $z/h = 0.30$, while $\Delta_{B,\tau} = 3.5°$ at $z/h = 0.03$ and $2.5°$ $z/h = 0.30$ for the A5 case. In other words, γ is larger by $\sim 3°$ when inferred from $R_{B,b}$ rather than from $R_{\tau,u}$.

The structures inferred from the inclination angles, superimposed on contoured fields of potential temperature deviations, are shown in Fig. 6 for cases A2–A5. This visualization was inspired by those presented in Sullivan et al. (2016). Since the authors in *op. cit.* used potential temperature, we employed the method described in (2017, Eq.12) to convert buoyancy at a given height to potential temperature deviations (relative to the planar mean). The inclined structures are readily evident in the potential temperature fields. The inferred structures computed using the cross-correlations and associated inclination angles align rather closely with the associated explicit structures. As stratification is increased, the flow becomes less turbulent, the boundary layer becomes shallower, and the inclined structures flatten in the middle-to-upper portions of the logarithmic region of the flow. The change in flow regime is especially noticeable in the A5 case. This alignment between the structures inferred from the inclination angle and those physically present in the flow seems to justify the use of the cross-correlation method in stratified boundary layers.

As discussed in Sect. 1, observational data concerning inclination angles of turbulent structures in stratified atmospheric boundary layers is sparse in the literature beyond, e.g., the few observations presented in Chauhan et al. (2013). In order to provide a more robust dataset with which to compare results from the DNS experiments presented in this study, we show new observational analysis from the Advection Horizontal Array Turbulence Study (AHATS; Salesky et al. 2012; Salesky and Chamecki 2012), which took place from 25 June to 16 August 2008 near Kettleman City, California. Inclination angles are computed following the same procedure as in Salesky and Anderson (2020), except selecting stable rather than unstable data. Angles are computed by calculating the two-point correlation from the six sonic anemometers mounted on the AHATS tower, and plotted against $z/L = z_2/L_2$ where $z_2 = 3.3$ m is the height of the second sonic anemometer and L_2 is the value of Obukhov length calculated at that height. Data is bin-averaged according to z/L. The associated data blocks are excluded if the wind components indicate non-stationarity or if the mean wind

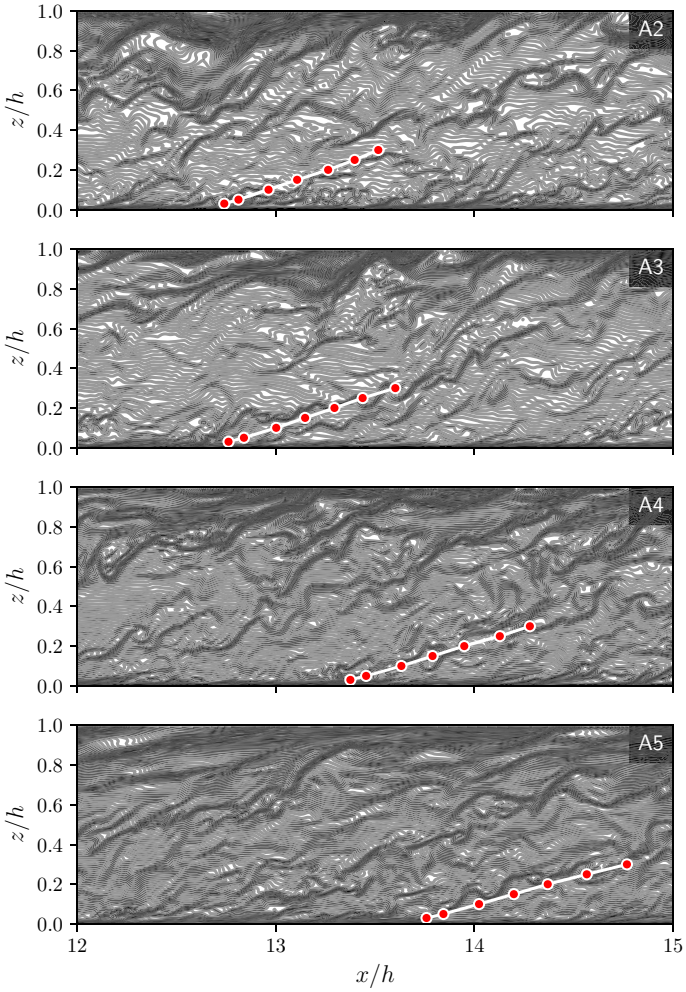

Fig. 6 Contoured temperature differences, with red points representing the inferred structures from the respective inclination angles computed using $R_{B,b}$

direction is more than 45° off-axis of the sonic anemometer to avoid flow distortion effects. In order for our DNS data to better align with the stability range of the AHATS data and to include the associated uncertainty information, the cross-correlation procedure outlined in Sect. 2.2 was amended in two ways. First, cross-correlations were computed using row samples instead of the full planar population, so that Eqs. (1) and (2) become:

$$R_{\tau,u}(\Delta_r, y, z) = \frac{1}{(N_x - 1)} \sum_{i=1}^{N_x} \frac{[\tau(x_i, y) - \overline{\tau}^x][u(x_i + \Delta_r, y, z) - \overline{u}^x]}{\sigma_\tau^x \sigma_u^x}, \tag{5}$$

and

$$R_{B,b}(\Delta_r, y, z) = \frac{1}{(N_x - 1)} \sum_{i=1}^{N_x} \frac{[B(x_i, y) - \overline{B}^x][b(x_i + \Delta_r, y, z) - \overline{b}^x]}{\sigma_B^x \sigma_b^x}, \tag{6}$$

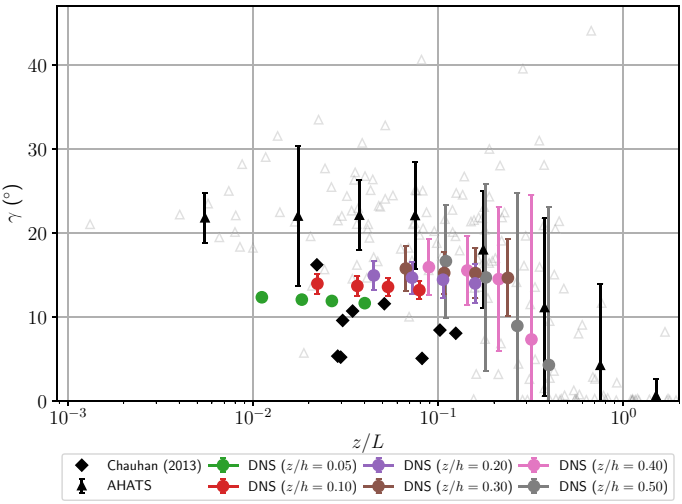

Fig. 7 Inclination angle versus stability. Diamonds are from Chauhan et al. (2013), triangles are from AHATS data (filled symbols are bin-averaged values), and circles correspond to DNS data taken at various z/h locations. Error bars indicate the standard deviation of the computed angle

where the x superscripts denote that means and standard deviations are computed with respect to the row sample. We confirmed that the considered statistics shown in Figs. 3, 4 and 5 did not change meaningfully or in a way that would alter the conclusions of the preceding sections. Second, we extended the statistical domain to a height of $z/h = 0.5$. Observational data from Chauhan et al. (2013) and AHATS are presented in Fig. 7 alongside our numerical output. On average, the DNS data generally fall between the two observational datasets. The AHATS and DNS data display similar behavior in that the angles remain fairly constant until $z/L \approx 0.1$, after which they decrease monotonically, and the associated variability increases with increasing stability.

4 Conclusions

There has been a robust history of studies exploring the form and properties of coherent structures in the ABL and other wall-bounded flows. This has often been explored through the lens of cross-correlations between the surface shear stress and the momentum above the underlying surface. The lag at which the maximum cross-correlations occur at a given height has been leveraged to construct the implied angles of these structures relative to the surface. While there have been extensive studies leveraging laboratory, observational, and numerical experiments for neutral and convective conditions, there has been a dearth of similar research focused on stable stratification. In this study, we conducted five large DNS runs of turbulent channel flow across a range of static stabilities to examine the inclination angles of coherent structures implied from the correlations of both surface shear stress with velocity and surface buoyancy flux with buoyancy. Additionally, we compared the numerical data with both the limited available observational data in the literature and observations from the AHATS field campaign.

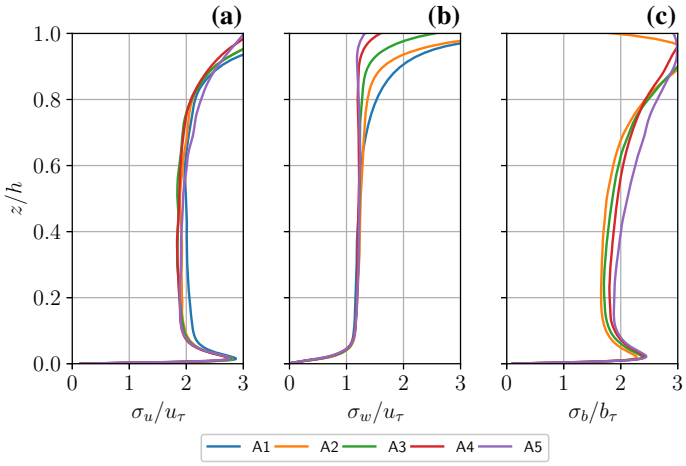

Fig. 8 Normalized standard deviations of **a** u, **b** w, and **c** b from a single snapshot during T_a^+. Here, $b_\tau = -B/u_\tau$

Results indicated that structures under stable stratification were at a lower angle relative to the surface than those under neutral conditions. We found that the angles of both momentum and buoyancy structures increased with height up to approximately $z/h = 0.15$, above which they either plateaued or decreased. Such a decrease is potentially associated with the so-called z-less stratification, in which normalized turbulence statistics using local scaling arguments are approximately constant with height (Wyngaard and Coté 1972). We show three such examples in Fig. 8, where normalized standard deviations of u, w, and b—taken from a single snapshot during T_a^+—are presented as functions of height. While not perfectly constant, they all are approximately so in the regions above $z/h = 0.15$ where the angles in Fig. 5 were shown to level off. Further, these approximately constant values of the normalized standard deviations are within the ranges reported in the literature (e.g., Basu et al. 2006; Grachev et al. 2013). Conversely, most of the Ri values presented in panel (f) of Fig. 1 at the top of the log region ($z/h = 0.3$) are not within the Ri-criteria for local z-less stratification ($0.1 < Ri, Ri_f < 0.20 - 0.25$) according to Grachev et al. (2013). However, this criteria is met across all stratified cases by $z/h = 0.6$. The behavior of the inferred angles may also point to effects associated with non-Kolmogorov turbulence such as intermittency.

We also found that the angles implied from buoyancy structures were larger than their momentum counterparts. Additionally, the effects of stratification were stronger near the top of the logarithmic region of the flow than in the near-surface region. Further, superimposing the implied angles computed from cross-correlations on structures visualized through potential temperature differences gave credence to the procedure for stable conditions. Finally, we demonstrated good agreement between observational and numerical data. Both showed that angles remain fairly constant until $z/L \approx 0.2$–0.3, after which they decrease montonically, and that the associated variability increased with increasing stratification. This behavior may indicate a separation line for which local z-less scaling behavior no longer exists. For instance, Pahlow et al. (2001) found that z-less behavior applied for $z/L \lesssim 0.1$, while Hong et al. (2010) found that z-less behavior was only observed up to $z/L \sim 0.5$. It may be that $0.1 \leq z/L \leq 0.5$ represents a transition zone away from z-less scaling, which would explain the behavior seen in Fig. 7.

The similar behavior of variability in the inclination angles between observations and DNS is a strong indication that such variability is related to physics of the flow and not a lack of data or data variability (e.g., different wind directions in AHATS data resulting in different angles). That is, this variability may be related to intermittency in stratified turbulence and the laminarization/bursting phenomena associated with such flows. One implication in terms of physical modeling is that as the flow becomes more stratified, LES surface boundary conditions will likely need to better capture this variability in order to properly represent instantaneous land-surface interactions. Additional observational and numerical experiments that extend the presented datasets across a broader range of stratifications and flow scenarios would prove helpful in further improving the understanding gained in the present study.

Acknowledgements This research was supported by the National Science Foundation under Grant AGS-1660367. The authors acknowledge high-performance computing support from Cheyenne (doi:10.5065/D6RX99HX) provided by NCAR's Computational and Information Systems Laboratory, sponsored by the National Science Foundation. The authors also wish to thank two anonymous reviewers for their helpful feedback. Data from this study are available from the corresponding author on reasonable request. The authors declare no conflicts of interest relevant to this study.

References

Adrian RJ (2007) Hairpin vortex organization in wall turbulence. Phys Fluids 19(4):041,301. https://doi.org/10.1063/1.2717527

Antonia RA (1981) Conditional sampling in turbulence measurement. Annu Rev Fluid Mech 13(1):131–156. https://doi.org/10.1146/annurev.fl.13.010181.001023

Basu S, Porté-agel F, Foufoula-Georgiou E, Vinuesa JF, Pahlow M (2006) Revisiting the local scaling hypothesis in stably stratified atmospheric boundary-layer turbulence: an integration of field and laboratory measurements with large-eddy simulations. Boundary-Layer Meteorol 119(3):473–500. https://doi.org/10.1007/s10546-005-9036-2

Boppe RS, Neu WL, Shuai H (1999) Large-scale motions in the marine atmospheric surface layer. Boundary-Layer Meteorol 92(2):165–183. https://doi.org/10.1023/a:1001837729368

Brown GL, Thomas ASW (1977) Large structure in a turbulent boundary layer. Phys Fluids 20(10):S243-s252. https://doi.org/10.1063/1.861737

Carper MA, Porté-Agel F (2004) The role of coherent structures in subfilter-scale dissipation of turbulence measured in the atmospheric surface layer. J Turbul 5:N40. https://doi.org/10.1088/1468-5248/5/1/040

Chauhan K, Hutchins N, Monty J, Marusic I (2013) Structure inclination angles in the convective atmospheric surface layer. Boundary-Layer Meteorol 147:41–50. https://doi.org/10.1007/s10546-012-9777-7

Computational and Information Systems Laboratory (2019) Cheyenne: Hpe/sgi ice xa system (climate simulation laboratory. https://doi.org/10.5065/D6RX99HX

Fedorovich E, Gibbs JA, Shapiro A (2017) Numerical study of nocturnal low-level jets over gently sloping terrain. J Atmos Sci 74(9):2813–2834. https://doi.org/10.1175/JAS-D-17-0013.1

García-Villalba M, del Álamo JC (2011) Turbulence modification by stable stratification in channel flow. Phys Fluids 23(4):045,104–22

Grachev AA, Andreas EL, Fairall CW, Guest PS, Persson POG (2013) The critical Richardson number and limits of applicability of local similarity theory in the stable boundary layer. Boundary-Layer Meteorol 147(1):51–82. https://doi.org/10.1007/s10546-012-9771-0

Heuer WD, Marusic I (2005) Turbulence wall-shear stress sensor for the atmospheric surface layer. Measurement Sci Technol 16(8):1644

Hong J, Kim J, Ishikawa H, Ma Y (2010) Surface layer similarity in the nocturnal boundary layer: the application of Hilbert–Huang transform. Biogeosciences 7(4):1271–1278. https://doi.org/10.5194/bg-7-1271-2010

Kim J, Moin P, Moser R (1987) Turbulence statistics in fully developed channel flow at low Reynolds number. J Fluid Mech 177:133–166. https://doi.org/10.1017/s0022112087000892

Liu HY, Bo TL, Liang YR (2017) The variation of large-scale structure inclination angles in high Reynolds number atmospheric surface layers. Phys Fluids 29(3):035,104. https://doi.org/10.1063/1.4978803

Lotfy ER, Harun Z (2018) Effect of atmospheric boundary layer stability on the inclination angle of turbulence coherent structures. Environ Fluid Mech 18(3):637–659

Mahrt L (1998) Nocturnal boundary-layer regimes. Boundary-Layer Meteorol 88(2):255–278. https://doi.org/10.1023/A:1001171313493
Marusic I, Heuer WDC (2007) Reynolds number invariance of the structure inclination angle in wall turbulence. Phys Rev Lett 99(114):504. https://doi.org/10.1103/PhysRevLett.99.114504
Marusic I, Kunkel GJ, Porté-Agel F (2001) Experimental study of wall boundary conditions for large-eddy simulation. J Fluid Mech 446:309–320. https://doi.org/10.1017/s0022112001005924
Mauritsen T, Svensson G (2007) Observations of stably stratified shear-driven atmospheric turbulence at low and high Richardson numbers. J Atmos Sci 64(2):645–655. https://doi.org/10.1175/JAS3856.1
Monin A, Obukhov A (1954) Turbulent mixing in the atmospheric surface layer. Tr Akad Nauk SSSR Geofiz Inst 24(151):163–187
Moser RD, Kim J, Mansour NN (1999) Direct numerical simulation of turbulent channel flow up to $Re_\tau = 590$. Phys Fluids 11(4):943–945. https://doi.org/10.1063/1.869966
Pahlow M, Parlange MB, Porté-Agel F (2001) On Monin-Obukhov similarity in the stable atmospheric boundary layer. Boundary-Layer Meteorol 99(2):225–248. https://doi.org/10.1023/A:1018909000098
Piomelli U, Ferziger J, Moin P, Kim J (1989) New approximate boundary conditions for large eddy simulations of wall-bounded flows. Phys Fluids A: Fluid Dyn 1(6):1061–1068. https://doi.org/10.1063/1.857397
Pope SB (2000) Turbulent flows. Cambridge University Press, Cambridge. https://doi.org/10.1017/CBO9780511840531
Rajagopalan S, Antonia RA (1979) Some properties of the large structure in a fully developed turbulent duct flow. Phys Fluids 22(4):614–622. https://doi.org/10.1063/1.862643
Richardson LF (1922) Weather prediction by numerical process. Cambridge Univ Press, Cambridge
Salesky ST, Anderson W (2018) Buoyancy effects on large-scale motions in convective atmospheric boundary layers: implications for modulation of near-wall processes. J Fluid Mech 856:135–168. https://doi.org/10.1017/jfm.2018.711
Salesky ST, Anderson W (2020) Revisiting inclination of large-scale motions in unstably stratified channel flow. J Fluid Mech 884
Salesky ST, Chamecki M (2012) Random errors in turbulence measurements in the atmospheric surface layer: Implications for Monin–Obukhov similarity theory. J Atmos Sci 69(12):3700–3714. https://doi.org/10.1175/JAS-D-12-096.1
Salesky ST, Chamecki M, Dias NL (2012) Estimating the random error in eddy-covariance based fluxes and other turbulence statistics: the filtering method. Boundary-Layer Meteorol 144(1):113–135. https://doi.org/10.1007/s10546-012-9710-0
Stoll R, Gibbs JA, Salesky ST, Anderson W, Calaf M (2020) Large-Eddy simulation of the atmospheric boundary layer. Boundary-Layer Meteorol 177(2):541–581
Sullivan PP, Weil JC, Patton EG, Jonker HJJ, Mironov DV (2016) Turbulent winds and temperature fronts in large-eddy simulations of the stable atmospheric boundary layer. J Atmos Sci 73(4):1815–1840
van Heerwaarden CC, vanStratum BJH, Heus T, Gibbs JA, Fedorovich E, Mellado JP (2017) MicroHH 1.0: a computational fluid dynamics code for direct numerical simulation and large-eddy simulation of atmospheric boundary layer flows. Geosci Model Dev 10(8):3145–3165
Venugopal V, Porté-Agel F, Foufoula-Georgiou E, Carper M (2003) Multiscale interactions between surface shear stress and velocity in turbulent boundary layers. J Geophys Res Atmos 108(D19)
Vinuesa R, Prus C, Schlatter P, Nagib HM (2016) Convergence of numerical simulations of turbulent wall-bounded flows and mean cross-flow structure of rectangular ducts. Meccanica 51(12):3025–3042. https://doi.org/10.1007/s11012-016-0558-0
Wyngaard JC, Coté OR (1972) Cospectral similarity in the atmospheric surface layer. Q J R Meteorol Soc 98(417):590–603. https://doi.org/10.1002/qj.49709841708